VisAdapt: Catadioptric Adaptive Camera for scenes of variable density of visual information

Julien Jean Ducrocq, Guillaume Caron, Hervé Midavaine, Christian Duriez, Jérémie Dequidt, El Mustapha Mouaddib

VisAdapt: Catadioptric Adaptive Camera for scenes of variable density of visual information

JULIEN DUCROCQ[1,2,*], GUILLAUME CARON[1,3], HERVÉ MIDAVAINE[1], CHRISTIAN DURIEZ[4], JÉRÉMIE DEQUIDT[4], AND EL MUSTAPHA MOUADDIB[1]

[1] *Université de Picardie Jules Verne (UPJV), MIS laboratory, 33 rue saint Leu, 80039 Amiens, France*
[2] *Nara Institute of Sciences and Technology (NAIST), CARE (Cybernetics and Reality Engineering) laboratory, B315 8916-5 Takayama-cho, Ikoma, Nara 630-0192, Japan*
[3] *CNRS-AIST JRL (Joint Robotics Laboratory), IRL, 1-1-1 Umezono, Tsukuba, Ibaraki, 305-8560, Japan*
[4] *Université de Lille, Inria, CNRS, Centrale Lille, UMR 9189 CRIStAL, F-59000 Lille, France*
[*] *julien.ducrocq.jz9@naist.ac.jp*

Compiled December 14, 2023

This paper presents the design method of a multi-resolution camera, named *Visadapt*. It is made of a conventional compact camera with a sensor and a lens pointed to a new deformable mirror so that the mirror at flat state is parallel to the image plane. The main novelty of the latter mirror is the ability to control automatically strokes of several millimeters. This allows Visadapt to capture scenes with a spatially variable density of visual information. A grid of linear actuators, set underneath the mirror surface, deforms the mirror to reach the desired shape computed to capture several areas of different resolutions. Mechanical simulations allowed to iterate on Visadapt's design, to reduce the geometrical distortions in the images. Evaluations made on an actual prototype of Visadapt show that, by adapting the mirror shape, this camera can magnify a scene object up to 20%, even off-centered in the field-of-view, while still perceiving the rest of the scene.

http://dx.doi.org/10.1364/ao.500663

1. INTRODUCTION

Everyday life environments are characterized by variety: they feature uniform regions, several objects and/or complex textures. Since they carry more visual information, objects and textures can be considered as key elements of the scene. Within such heterogeneous environments, the density of visual information is spatially variable. Therefore, when they are captured by a conventional camera, uniform scene regions may use the majority of the pixels and key elements of the scene only a few pixels (Fig. 1a). Thanks to the optical zoom, classical cameras increase the resolution of a specific region of the scene by increasing their focal length [1]. Nonetheless, the objects which are not targeted by the zoom are not visible anymore (Fig. 1b versus Fig. 1a).

Several applications are impacted by heterogenous environments. In robotics, visual servoing methods [2, 3] allow mobile robots to navigate only with visual information. If the scene is made of wide uniform regions, the robot trajectory may fall under local minima tens of centimeters away from the desired location due to the lack of features [4, 5]. Moreover, in video-surveillance, faces or silhouettes may not occupy enough pixels to allow identification. A pan-tilt-zoom (PTZ) camera may zoom-in a person to capture enough information for identification [6, 7], but it would not be able to monitor the rest of the scene anymore.

(a) Image captured with a conventional lens

(b) Image captured with a longer focal than (a)

(c) Multi-resolution image

Fig. 1. Different images of an heterogeneous environment. The area framed in red occupies less pixels in (c) than in (a), while the rest is zoomed.

Thus, in these contexts, a camera should capture images with a locally variable angular resolution, to make key scene elements occupy more pixels than uniform regions that could shrink to a few pixels. For this purpose, such a camera has to capture $P \in \mathbb{N}$ scene regions, each with a desired resolution, leading to a multi-resolution image (Fig. 1c). Furthermore, instead of tailored for a specific static scene, the local resolution of this camera needs to adapt to different scene geometries for versatile uses. Conceptually, such camera could be implemented with either a large pixel density followed by hardware local binning, spatially variable image sensor with photodiodes of adaptive sizes, or a deformable optical surface. We focus on the latter because the first is bounded by the noise of tiny photodiodes [8], no local hardware binning technology exists, and the second is not available yet. Deformable lenses *e.g.* electrowetting lenses [9], only change the magnification globally [10] or defocus blur,

locally [11]. Therefore, we propose to design and actuate an optical surface centimeters away the camera chip: a deformable mirror, facing a conventional camera.

The new catadioptric camera is named Visadapt. Its mirror is made of a thin reflective surface above a matrix of linear actuators, and its shape is adaptively optimized to capture a desired spatially variable resolution. The design of Visadapt has been iteratively improved thanks to mechanical simulations to reach the smooth curvatures of the ideal deformed optical surface, hence limiting the geometrical discontinuities of the captured images. Simulation results, completed by experiments on a proof-of-concept prototype, show that Visadapt is able to capture multi-resolution images with up to nine contiguous scene regions of different resolutions.

In the rest of this article, Section 2 relates the cameras who inspired Visadapt's design and existing methods to optimize a mirror shape. Then, Section 3 describes the design method of Visadapt involving mechanical simulations of deformable materials and optical geometry. After that, Section 4 reports and evaluates results with simulated scenes and Section 5 validates the practical design by images captured with a deformable mirror prototype, before Conclusion (Sec. 6).

2. RELATED WORKS

Adaptive cameras The adaptive cameras we consider are those able to change optical properties across time with hardware adaptation at the image capture time, contrary to cameras such as plenoptic cameras [12] that capture the light-field for software adaptation as post-processing Among them, several are related to Visadapt's purpose. Adaptive cameras with a grid of deformable lenses can change their FOV [13] or magnification [14] globally. Thanks to several layers of pinhole grids, a lensless camera [15] is able to capture up to nine scene regions, each with a different magnification, but all the areas in between are lost. Moreover, a conventional camera facing a bendable mirror, can capture images with a non-uniform resolution [16]. The deformations of the latter consist in manual global bending of a few centimeters. Conversely, the deformable mirrors (DMs) used in the context of adaptive optics [17–19] are automatically controllable and capable of multiple local deformations. But since they modulate the optical phase of light beams in the entire FOV to increase locally the sharpness of images, they deform at high frequency of up to tens of micrometers. Thus, the image geometry is not changed by adaptive optics' DMs.

Mirror shape optimization Several methods exist to design a static mirror shape to capture scene regions with a desired resolution, *e.g.* with vector fields [20] or polynomial functions [21]. [22] computes b-splines-based mirror surfaces, which reflect light rays from scene points to desired pixel locations on the camera image sensor, matching a *scene-to-image* mapping. On the one hand, optimized mirrors are made once, *e.g.* to be put in cars for the driver gaze check while observing the surrounding road [20], or to be put at the center of crossroads for traffic monitoring [21]. On the other hand, existing DM-based adaptive cameras are aimed to capture astrophotographs [18] or retinal images [23], requiring a μm-scale stroke at high frequency.

3. THE DESIGN OF VISADAPT

Visadapt combines a DM of centimeters stroke (as the manually flexible mirror [16]) with an automatic actuation, to locally modify the image geometry. It is the first controllable camera able to magnify several scene regions at once within a multi-resolution image, without omitting any object within the camera FOV (unlike *e.g.* lensless cameras with several pinhole grid layers [15]). When the scene changes, a new mirror surface can be computed with b-splines optimization [22] , then the actuators will deform Visadapt's mirror to reach the optimal surface, *e.g.* to better emphasize the objects featuring more visual information.

A. The scene-to-image mapping model

Visadapt aims at capturing a scene with a desired spatially variable resolution, hence satisfying a *scene-to-image* mapping $\mathcal{M}$ (which projects a scene point $\mathbf{X} = (X, Y, Z)^T \in \mathbb{R}^3$ to an image pixel $\mathbf{U} = (U, V) \in \mathbb{R}^2$). Fig. 2 illustrates the path of a light ray from $\mathbf{X}$ to $\mathbf{U}$. Incident light rays $\mathbf{V}_i \in \mathbb{R}^3$ from scene points $\mathbf{X}$ intercept the mirror surface $\mathcal{S}$ at $\mathbf{X}_m = (X_m, Y_m, Z_m)^T \in \mathbb{R}^3$, and then are reflected as $\mathbf{V}_r \in \mathbb{R}^3$. The coordinates of all these points are expressed within the camera orthonormal frame $\mathcal{F}_c = \{{}^c\mathbf{X}, {}^c\mathbf{Y}, {}^c\mathbf{Z}\}$.

$\mathbf{V}_r$ is expressed with the local normal $\mathbf{N}_m = (N_x, N_y, N_z)^T \in \mathbb{R}^3$ to the mirror surface at $\mathbf{X}_m$, following the Snell-Descartes law $\mathbf{V}_r = \mathbf{V}_i - (2\mathbf{N}_m^T\mathbf{V}_i)\mathbf{N}_m$. If $\mathcal{S}$ is optimized to satisfy $\mathcal{M}$, the real image plane coordinates $\mathbf{x} = (x, y, z)^T \in \mathbb{R}^3$ of the desired pixel $\mathbf{U} = (U, V)$ will belong to $\mathbf{V}_r$.

To simplify, consider the scene as P co-planar scene regions made of $m_p \times n_p \in \mathbb{N}$ points of metrical known positions $\mathbf{X}$, delimited by borders $\mathbf{X}_{p-}$, $\mathbf{X}_{p+} \in \mathbb{R}^3$, with $p \in [0,\ P] \subset \mathbb{N}$. The image captured, $\mathbf{I}$, is made of P sub-images $\mathbf{I}_p$, each capturing a scene region p by $m_p \times n_p$ pixels, of desired location $\mathbf{U}$ in between borders $\mathbf{U}_{p-}$, $\mathbf{U}_{p+} \in \mathbb{R}^2$. $\mathbf{I}$ is a multi-resolution image if at least one couple of sub-image borders $\mathbf{U}_{p-}$, $\mathbf{U}_{p+}$ does not match the pinhole projection of the corresponding scene borders $\mathbf{X}_{p-}$, $\mathbf{X}_{p+}$. Indeed, it implies that the catadioptric camera can be modeled as P sub-cameras, with different intrinsic parameters $\Gamma_p = (k_{u_p}, k_{v_p}, u_{0_p}, v_{0_p}) \in \mathbb{R}^4$ (k_{u_p}, k_{v_p} are the pixel size and u_{0_p}, v_{0_p} are the coordinates of the principal point for each subcamera p). In order to capture an image of a non-uniform resolution, the mirror of a catadioptric camera must have curvatures [20, 22], so does Visadapt's mirror.

To satisfy $\mathcal{M}$, $\mathcal{S}$ is optimized iteratively, *e.g.* by minimizing the residual errors between a set of desired normals $\mathbf{N}_m^* \in \mathbb{R}^3$, each associated with a couple $(\mathbf{X}, \mathbf{U})$, and the local tangent of $\mathcal{S}$, $\mathbf{T}_m \in \mathbb{R}^3$ [22]. For the first iteration, the mirror is initially assumed planar. Then, all $\mathbf{N}_m^*$ are recomputed for each iteration, considering the mirror surface obtained at the end of the

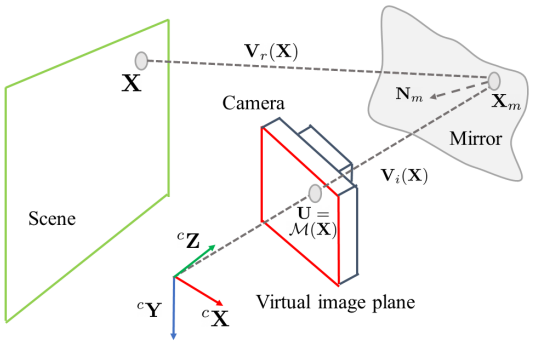

Fig. 2. The path of a light ray through the scene-to-image mapping (from the scene to the image sensor).

previous iteration, generally not planar.

B. The core idea of the design

In order to reach the optimal surface $\mathcal{S}$, Visadapt uses a deformable mirror made of a reflective membrane with a matrix of $R \times C \in \mathbb{N}$ linear actuators underneath, regularly spaced, each one moving along the normal to the mirror in planar state. The number of actuators $R \times C$ is chosen as a compromise between the resolution of actuation and the compactness of the design. The actuators are considered completely rigid, whereas the mirror surface is considered flexible enough to be locally deformed by an underneath push actuation. Visadapt relies on several parameters, which have been assessed through mechanical simulations and formally described thereafter.

C. Design parameters evaluated through simulation

Thanks to a realistic mechanical simulation, several parameterized configurations of the mirror can be compared, to assess their impact on the mirror reflection and chose an optimal design for the prototype. A first parameter, the actuation surface ($S_a \in \mathbb{R}$, expressed in mm^2) changes the geometry of the contact area between the actuator and the mirror surface. This parameter has a strong impact on the local shape of the deformations. Then, in order to smooth the curvature of the mirror, a layer of a flexible material (referred here as a *smoothing layer*) is added between the mirror membrane and the actuators heads. The reflection will therefore depend on the thickness $e \in \mathbb{R}_+^*$ of this layer, a second critical design parameter.

It is worth noting that the mechanical model includes several other parameters for the reflective membrane that are its thickness, its elasticity, the clamping model to a frame and the resulting tensile stress. However, they are set constant such as, according to the rectangular aspect of an image, the shape of the frame is set rectangular and the clamping of the membrane to the frame is modeled as dense fixed-point constraints along the four sides of the frame and the resulting tensile stress is neglected to not modify the mirror membrane elasticity parameter. Indeed, Section 5 reports that a single mirror membrane product was found to reach a satisfying visual quality, and describes as well the practical details that allow to make these above-mentioned assumptions realistic.

A poor choice of the actuation surface S_a and the smoothing layer thickness e would lead the images captured with the Visadapt camera to show many distortions. Hence, S_a and e will be chosen minimizing the distortions in the image thanks to a simulation which scene considers a chessboard made of $j \times k \in \mathbb{N}^*$ squares, set fronto-parallel to the image, their axes aligned (Fig. 3b). In the simulation, a mapping $\mathcal{M}$ is set to reduce the resolution of the central scene region, hence increasing the resolution of every other region. To make the target area reach the desired resolution, an optimal mirror shape (Fig. 3a) is computed at first using b-splines surface optimization [22] with default parameters, that are $nb_K = 36$ knots, splines of order $m_{ord} = 5$ and the number of iterations $n_{iter} = 3$ (thanks to the Matlab *Reflex* toolbox of [22]). Then, the actuator heights $h \in \mathbb{R}$ are computed as the intersection of the actuator axes (see the black bars of Fig. 3a) and the optimal mirror shape (Fig. 3a). h also considers the smoothing layer thickness and that only push actuations ($h > 0$) are considered with the Visadapt prototype (Sec. 5).

Afterwards, $S \in \mathbb{N}$ virtual models of the deformable mirror (considering different values of S_a and e) are actuated and set in front of a virtual camera to the scene reflection thanks to ray tracing within the Unity® rendering engine. Since the command is a desired image grid, we evaluate the mirror through its reflection of the scene. We thus quantify the undesired distortions within the S images obtained, $\widehat{\mathbf{I}}_s$, $s \in [0,\ S-1] \subset \mathbb{N}$, by leveraging the TV distortion measure of the ISO 9039 [24]. It is easy to use here since the chessboard is fronto-parallel to the virtual camera image plane and the chessboard axes are parallel to those of the image. However, the TV distortion method measures a percentage of global distortion that the curvy side of the chessboard shows in the image with respect to the straight line it should be. So, to deal with the local distortions that Visadapt images can show and to provide a single distortion measure for the whole chessboard instead of one per chessboard side, we extend the TV distortion method as follows. First, we do not only consider the chessboard borders but all $L = (j-1) + (k-1) \in \mathbb{N}^*$ vertical and horizontal lines other than the chessboard borders to account for local distortions. Then, we measure the distortions with every pixel of each line $l \in [0,\ L-1]$, each pixel being automatically detected thanks to Sobel's edge detection, as the horizontal standard deviation σ_{h_l} of all pixels corresponding to a vertical line l, respectively the vertical standard deviation σ_{v_l} of all pixels corresponding to a horizontal line l. Finally, to output a single distortion measure for the whole chessboard, we compute $\Delta \in \mathbb{R}_+^*$ as the mean of all σ_{h_l} and σ_{v_l} for all lines l. With such extensions to the seminal TV distortion method, the percentage representation has no more meaning and is thus dropped, but anyway the lower Δ the least the distortions. This quantitative evaluation is completed by the qualitative assessment of the image in general (*e.g.* locating visually where the image suffers more important local distortions).

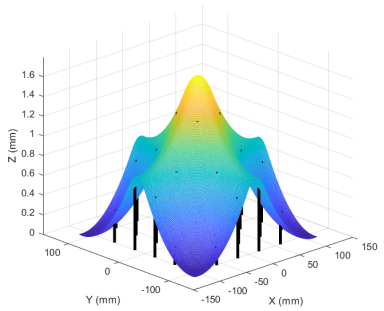

(a) Mirror surface and actuators underneath (represented as black bars).

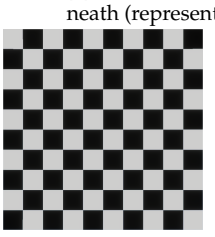

(b) The chessboard scene.

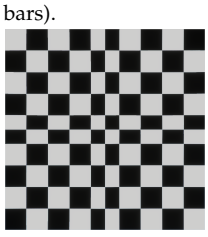

(c) The scene reflection through the optimal mirror surface.

Fig. 3. The optimal mirror with the actuators underneath and the scene tested for the simulation experiments.

D. Evaluation method

To evaluate the ability of Visadapt to reach mappings $\mathcal{M}$, we introduce $\eta \in \mathbb{R}$ characterizing the ratio between the desired resolution of the area of interest and its reflected image resolution. Writing $n^* \in \mathbb{N}^+$ the desired number of pixels in the target area (its desired definition), and $\hat{n} \in \mathbb{N}^*$ the actual number of pixels in the corresponding area in the image reflected by the mirror, η is defined as follows:

$$\eta = \frac{n^*}{\hat{n}} \,. \tag{1}$$

The closer η is to 1.0, the more faithful is the mirror w.r.t. the mapping $\mathcal{M}$. η is considered to evaluate both simulation and experimental results with the final design.

4. MECHANICAL SIMULATION TO DETERMINE THE DEFORMABLE MIRROR PARAMETERS

This section presents, first, the simulation environment, then, the materials and the geometrical configuration of Visadapt, before results for various actuation surfaces and smoothing layers. Afterwards, another set of results on a scene other than a chessboard proves the ability of the virtual Visadapt to reach several *scene-to-image* mappings $\mathcal{M}$, thanks to the actuators changing the mirror shape.

For the first evaluation, the criterion Δ (Sec. D) quantifies the distortions of $L = 18$ inner lines (see Fig. 4), consisting in 9 horizontal lines (in green) and 9 vertical lines (in red). To detect those lines without outliers, the intensity threshold of the Sobel's edge detection is manually set to $\epsilon = 0.2$.

A. Simulation environment

Actuators are modeled as rigid moving objects. Finite Element Method is used for the deformations of the mirror. Some bilateral constraints [25] allow to model the interactions between the motors and the mirror. Our mechanical simulation is using the Sofa framework, an open-source and realistic mechanical simulator. For a single simulation step, the actuators change of heights, then an Euler implicit solver [26] computes local forces to deform realistically the mechanical model of the mirror [27], until they reach their final height.

At the end of the mechanical simulation, to compute realistic reflections thanks to ray tracing, the surface of the deformable mirror is transferred to a virtual environment, here rendered with the Unity® engine. Within this virtual environment, the camera is set at the origin of the world frame, the scene plane is set at $Z_{scn} < 0$ away from the camera and the mirror (initially planar) at $Z_{mir} > 0$. The camera image plane, the scene plane and the mirror are all parallel such that the flat mirror leads to a perspective image. In the simulations, we set $Z_{scn} = -150\ mm$ and $Z_{mir} = 396\ mm$, such that the whole experimental volume will be easy to reproduce for the prototype in the laboratory, with a camera which captures images of 1000×1000 pixels, and of intrinsic parameters $\Gamma_c = (k_u, k_v, u_0, v_0)$, with $k_u = k_v = 0.047\ mm$, and $u_0 = v_0 = 499.5\ pixels$ and of focal length $f = 8\ mm$.

B. The materials of Visadapt

Available servomotors are made of a rigid material, which cannot be deformed. Within the mechanical simulation, the properties (especially Poisson's ratio $\nu \in \mathbb{R}_+$ and Young's modulus $E \in \mathbb{R}_+^*$) of all the different materials must be specified, except for the fully rigid actuators.

In order to determine the material of the mirror membrane, we tested several sheets of reflective materials, *i.e.*, a 1.0 mm thick sheet of Polyvinyl chloride (PVC), a 0.20 mm thick polyethylene terephthalate (PET) adhesive sheet and a 0.12 mm thin PET sheet. Each of them is covered by a thin layer of silver. For a local actuation, performed by a single actuator, underneath, only the thin PET sheet is deformed locally, the thicker PET and PVC sheets globally change of curvature, thus cannot be considered for the Visadapt prototype. Since we use PET, to ensure that the mirror membrane is initially planar and of the highest reflection quality, it must be tensed by a rigid frame (otherwise the scene objects are distorted by the reflection, see Fig. 7a versus Fig. 7b).

The PET is characterised by a Young's modulus of $E = 3.5\ GPa$ and a Poisson's ratio of $\nu = 0.38$. For the smoothing layer, we consider a more deformable material, to enable the mirror of Visadapt to reach diverse shapes, here the silicone rubber, of $E = 25\ MPa$ and $\nu = 0.48$. In order to enlarge the actuation base, a square pad, made of polypropylene, is added to the head of each actuator, a material defined by $E = 1.325\ GPa$ and $\nu = 0.43$.

C. The configuration of the deformable mirror

As a compromise between resolution of actuation, compactness, the amount of electronic interfaces and available products, we set $R = C = 6$ to reach 36 actuators that have a $5\ mm \times 5\ mm$ square base. They are regularly spaced on a grid of $230\ mm \times 230\ mm$, of 46 mm step size, which leads to $f = 8\ mm$ to ensure that the camera (with a CMOS of about $5.9\ mm \times 4.8\ mm$) at $Z = 0$, perceives all the actuators (set at $Z_{mir} = 396\ mm$) at once. The rigid frame is set as far as possible from the actuated area to limit the constraints on the actuation while keeping a reasonable size. Within the virtual environment, this frame is modelled as fixed constraints on the four borders of the mirror.

To create a virtual deformable mirror, a mesh made of hexahedra gathers the actuators, the thin mirror surface and, when necessary, the smoothing layer. The actuators are rigidly attached to the smoothing layer (or the mirror surface directly). This mesh is used as a mechanical model which can be deformed within the simulation. To prepare the simulations, each part of the mesh is associated to different mechanical properties, such as Young's modulus and Poisson's ratio, to make a realistic mechanical model, apart from the actuators which are completely rigid (see Sec. B).

D. Impact of the actuation surface

Within the mechanical model, the impact of the actuation surface S_a is measured, for three different values $S_a \in \{5 \times 5\ mm^2,\ 20 \times 20\ mm^2,\ 30 \times 30\ mm^2\}$. When the actuation surface is small, the $5 \times 5\ mm^2$ square head of the actuator is directly touching the mirror membrane, inducing undesired local discontinuities severely distorting the captured image (Fig. 4a). As the actuation surface grows, the lines get less distorted, as shown in Fig. 4b-4c. Indeed, the criterion Δ is, respectively, of 2.81, 2.27 and 1.58 pixels: Δ decreases linearly as S_a increases. Nonetheless, for any S_a tested, the borders of the square pads enlarging the actuation surface still induce distortions. These results emphasize the need to add a smoothing layer in between the actuators and the mirror membrane.

E. Impact of the smoothing layer thickness

The goal of the smoothing layer is to attenuate the discontinuities of the mirror and reduce the geometrical distortions within the

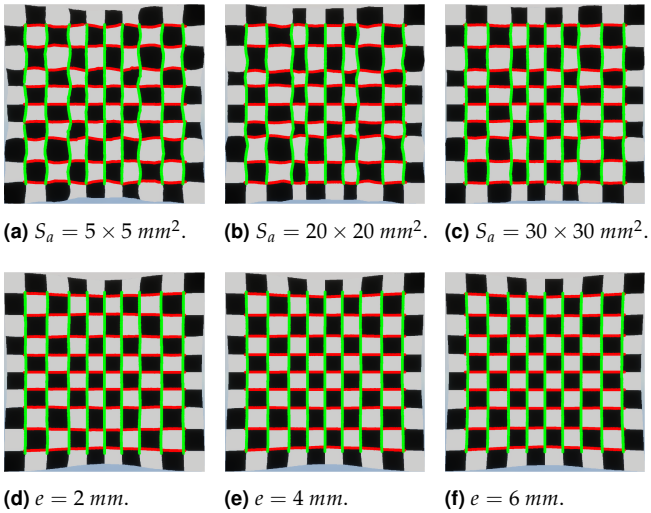

(a) $S_a = 5 \times 5\ mm^2$. **(b)** $S_a = 20 \times 20\ mm^2$. **(c)** $S_a = 30 \times 30\ mm^2$.

(d) $e = 2\ mm$. **(e)** $e = 4\ mm$. **(f)** $e = 6\ mm$.

Fig. 4. Reflection of the chessboard for 3 different actuation surfaces S_a and 3 different smoothing layer thicknesses e.

image captured. Thicknesses $e \in \{2\ mm, 4\ mm, 6\ mm\}$ have been successively tested, while the actuation surface remains $S_a = 30 \times 30 mm^2$ (the less distorting, Sec. D). When considering all the 18 chessboard lines detected, the criterion Δ changes for each e, reaching successively 1.53, 1.26 and 1.40 pixels. Since the borders of the mirror membrane are constrained by the virtual frame, the smoothing layer has a different impact in the center than in the border of the image. On the one hand, the image borders display scene regions outside of the initial camera field of view, of which areas increase as the thickness of the smoothing layer (see the three reflection images on the second line of Fig. 4). On the other hand, for the 10 lines of the 4×4 central squares, the distortions decrease as the smoothing layer gets thicker, Δ being successively of 0.65, 0.49 and 0.42 pixels. Even though the central region is less distorted for the thickest smoothing layer, the reflected image suffers less distortions with $e = 4\ mm$.

For the simulations of the rest of this section and the design of the actual prototype, we consider an actuation surface of $S_a = 30 \times 30\ mm^2$ and a smoothing layer thickness of $e = 4\ mm$.

F. Ability to reach diverse scene-to-image mappings

In this section, we consider two different mappings $\mathcal{M}_1$ and $\mathcal{M}_2$. One simulation is done for each mapping, where the ability of Visadapt to capture a desired multi-resolution image is assessed by the criterion η (Sec. D) computed on the reflection of the deformed mirror. The scene used here is a photograph of the cathedral of Amiens, an environment with heterogenous densities of visual information, since it features many statues of different sizes and uniform areas of flat stone.

$\mathcal{M}_1$ and $\mathcal{M}_2$ change the resolution of a target area, respectively starting at coordinates $\mathbf{U}_1 = (300, 300)$ and $\mathbf{U}_2 = (480, 415)$, from 400×400 pixels to 300×300 pixels and from 200×200 pixels to 150×150 pixels. $\mathcal{M}_1$ and $\mathcal{M}_2$ are illustrated by Fig. 5: Fig. 5a and Fig. 5c represent the conventional images, acquired by the camera facing a planar mirror, and Fig. 5b and Fig. 5d represent the multi-resolution desired images. Since $\mathcal{M}_1$ and $\mathcal{M}_2$ decrease the resolution of the target area (red areas in Fig. 5) by the same horizontal and vertical factor, the resolution of the areas at the four corners of the FOV increase too. About the four remaining regions (central top and bottom, middle right and left) they are transformed differently: on the one hand, the left and right regions are shrunk vertically but enlarged horizontally; on the other hand, the top and bottom regions are shrunk horizontally but enlarged vertically.

$\mathcal{M}_1$ projects a centered scene region through a centered image region, therefore, the corresponding optimal mirror shape computed with [22] is symmetrical, with a high convexity at its center and small convexities at its borders (Fig. 6a). The mapping $\mathcal{M}_2$ considers a scene area which is not centered, therefore, the mirror shape (Fig. 6c) is not symmetrical anymore, and all the points on approximately one fourth of the mirror are characterized by $Z \approx 3.0\ mm$.

For $\mathcal{M}_1$, the mirror reflection is still captured as a multi-resolution image (Fig. 6b), but it suffers from distortions on its borders (caused by the frame countering the larger actuation on the borders). However, the target area is quite faithful to the desired one, since $\eta = 1.1$. For $\mathcal{M}_2$, since several actuators on the borders are set to 3 mm of height, but are constrained by the frame nearby, the borders of the image suffer high distortions. However, the target area, close to the center, is less affected, and changes of resolution to reach 174×182 pixels ($\eta \approx 1.19$).

In summary, within the mechanical and visual simulation, Visadapt allows capturing multi-resolution images close to the desired ones, η being from 1.1 to 1.19 in the considered examples, even though the images suffer from off-center distortions.

5. PROTOTYPE AND RESULTS

This section introduces the prototype of Visadapt and shows preliminary results of image capture, as a proof-of-concept confirming the design decisions made following the simulation study.

A. The actual prototype of Visadapt

The prototype of Visadapt (Fig. 7) is based on the results obtained through the simulations reported in Section 4. The dimensions match the description of Section C, and the respective locations of the camera, the mirror and the scene remain as in Section A. Moreover, Visadapt is made of the materials listed in Section B.

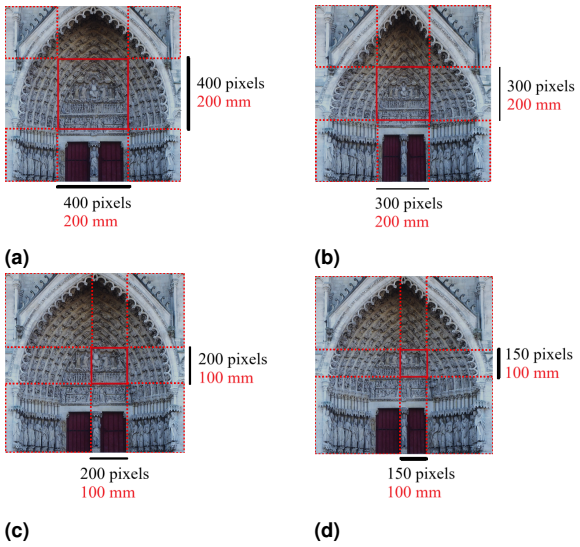

Fig. 5. Conventional (Fig. 5a and 5c) and desired (Fig. 5b and 5d) multi-resolution images (the target area is framed in red). Whereas the first line corresponds to the scene-to-image mapping $\mathcal{M}_1$, the second illustrates the mapping $\mathcal{M}_2$.

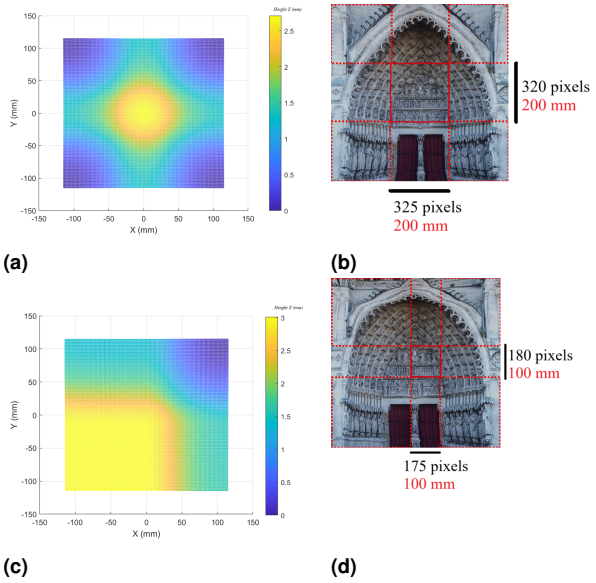

Fig. 6. For the two mappings $\mathcal{M}_1$ (first line) and $\mathcal{M}_2$ (second line), X-Y view of the optimal mirror shapes (a,c) and ray traced reflections, through the actuated mirror, of the scene, with the target area (defined in Fig. 5) framed in red (b,d).

For the prototype, we used servomotors Actuonix® PQ12 which move linearly along a main axis, on a 20 mm range. In order to enlarge the actuation base, a 30 $mm \times 30$ mm square pad is added to the head of each actuator (see Sec. B). The pads are not rigidly attached to the 4 mm thick silicone smoothing layer. There is no issue when pushing nor when the actuator moves back to its minimal height since the smoothing layer is between the actuators grid and the tensed PET sheet. The PET sheet is tensed by a rigid frame along the four borders of the sheet (see Fig. 7a and Fig. 7b for a comparison between reflection of relaxed and tensed PET sheets).

Practically, the prototype of Visadapt can be modified easily with a different number of actuators, thanks to a latch that also allows to easily change the silicone sheet used as a smoothing layer.

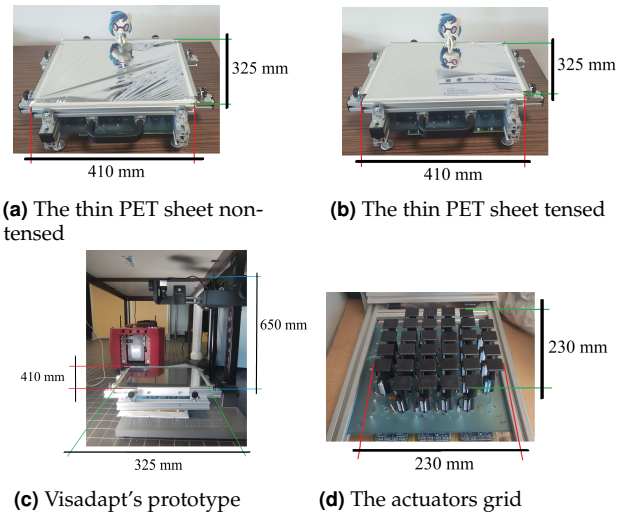

(a) The thin PET sheet non-tensed

(b) The thin PET sheet tensed

(c) Visadapt's prototype

(d) The actuators grid

Fig. 7. The deformable mirror, the prototype of Visadapt and the actuators grid.

B. Results

The prototype is facing a planar scene made of the logos of the three laboratories involved in this project, placed on three different corners of the field-of-view (Fig. 8a). For this experiment, we consider the *scene-to-image* mapping $\mathcal{M}_3$, which reduces the target area definition of 20%, from 500×500 pixels to 400×400 pixels (Fig 8b). Subsequently, the resolution of the four corners of the captured field-of-view increases from 250×250 pixels to 300×300 pixels.

The mapping $\mathcal{M}_3$ is considered to compute the optimal shape that the deformable mirror should reach. The shape computed with b-splines [22] is mainly convex, with an actuation up to 2.5 mm (Fig. 8d). The image captured by the prototype (Fig. 8c) indeed reduces the resolution of the target area to 440×440 pixels. Therefore, $\eta = 1.1$, the resolution of the target area is 10% higher than the desired one. Moreover, the three logos are respectively magnified by $G_1 = 1.20$ (for the JRL logo), $G_2 = 1.15$ (for the MIS logo) and $G_3 = 1.08$ (for the CRIStAL logo), highlighting the spatially variable resolution of the image. These results confirm that Visadapt is able to capture images with an adaptive local resolution.

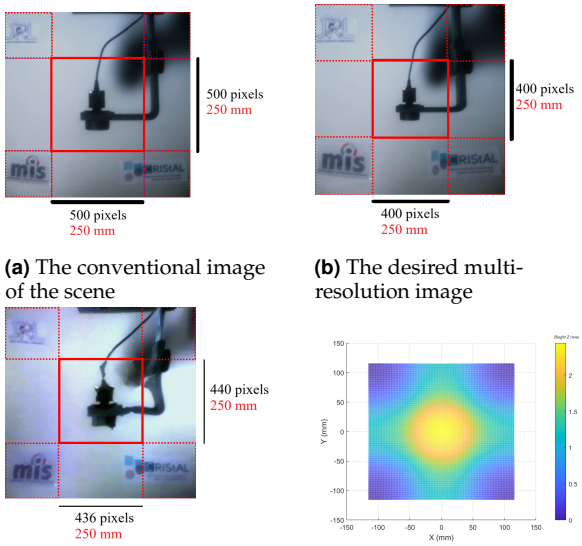

(a) The conventional image of the scene

(b) The desired multi-resolution image

(c) The scene reflected by the deformed mirror

(d) The shape of the deformed mirror

Fig. 8. Experiments with the prototype, images of the scene captured, with the target area framed in red, and the computed mirror shape.

6. CONCLUSION AND FUTURE WORKS

To capture more visual information in environments of heterogeneous density, we designed an adaptive multi-resolution catadioptric camera, Visadapt, by introducing a new deformable and controllable mirror, a tensed PET sheet deformed by a grid of servomotors, in front of a conventional camera. The new camera was iteratively co-designed with realistic mechanical simulations to select proper materials and refine the geometry of elements interfacing them. Results of the first prototype show that Visadapt is able to magnify several disjoint areas at once, increasing by 20% the resolution of off-centered parts of the

field-of-view, without losing any intermediary area, of course shrinking the resolution of the latter.

In order to take full benefit of its dynamic adaptation potential, future works aim at reducing the size of the Visadapt prototype in order to mount it on mobile robots, *e.g.* to improve autonomous navigation in challenging environments where large areas are uniform and a few are visually rich.

Funding. The work presented in this paper has been partially funded by Amiens métropole, the French Ministère de l'Enseignement Supérieur et de la Recherche (MESR) and by the "Visadapt" project, CNRS INSIS PEPS 2021-2022.

Acknowledgments. We would like to thank Rayane Méchik, a Master student at Polytech Lille, for the technical support he gave to this project during his internship at CRIStAL.

Disclosures. The authors declare no conflicts of interest.

Data Availability Statement. No data were generated or analyzed in the presented research.

REFERENCES

1. H. Maître, *From photon to pixel: the digital camera handbook* (John Wiley & Sons, 2017).
2. G. Caron, E. Marchand, and E. M. Mouaddib, Auton. Robots **35**, 177 (2013).
3. J. Gaspar and J. Santos-Victor, "Visual path following with a catadioptric panoramic camera," in *IEEE Int. Symp. on Intelligent Robotic Systems,* (1999), pp. 139–147.
4. M. Sheckells, G. Garimella, and M. Kobilarov, "Optimal visual servoing for differentially flat underactuated systems," in *IEEE/RSJ Int. Conf. on Intelligent Robots and Systems,* (2016), pp. 5541–5548.
5. X. Sun, X. Zhu, P. Wang, and H. Chen, "A review of robot control with visual servoing," in *IEEE Annual Int. Conf. on Cyber Technology in Automation, Control, and Intelligent Systems,* (2018), pp. 116–121.
6. P. Kumar, A. Dick, and T. S. Sheng, "Real time target tracking with pan tilt zoom camera," in *IEEE Digital Image Computing: Techniques and Applications,* (2009), pp. 492–497.
7. R. Cucchiara, A. Prati, R. Vezzani *et al.*, "Advanced video surveillance with pan tilt zoom cameras," in *IEEE Int. Workshop on Visual Surveillance,* (2006), pp. 334–352.
8. J. Goy, B. Courtois, J. Karam, and F. Pressecq, Analog. Integr. Circuits Signal Process. **29**, 95 (2001).
9. C. Quilliet and B. Berge, Curr. Opin. Colloid & Interface Sci. **6**, pp. 34 (2001).
10. L. Li, D. Wang, C. Liu, and Q.-H. Wang, Opt. express **24**, pp. 2931 (2016).
11. G. S. Jung and Y. H. Won, Appl. Opt. **59**, pp. 5527 (2020).
12. M. Levoy, Computer **39**, 46 (2006).
13. D. C. Sims, Y. Yue, and S. K. Nayar, "Towards flexible sheet cameras: Deformable lens arrays with intrinsic optical adaptation," in *IEEE Int. Conf. on Computational Photography,* (2016), pp. 1–11.
14. D. C. Sims, O. Cossairt, Y. Yu, and S. K. Nayar, arXiv preprint 1804.07052 (2018).
15. A. Zomet and S. K. Nayar, "Lensless imaging with a controllable aperture," in *IEEE Conf. on Computer Vision and Pattern Recognition,* , vol. 1 (2006), pp. 339–346.
16. S. Kuthirummal and S. K. Nayar, "Flexible mirror imaging," in *IEEE Int. Conf. on Computer Vision,* (2007), pp. 1–8.
17. R. Freeman and J. E. Pearson, Appl. Opt. **21**, 580 (1982).
18. R. Davies and M. Kasper, Annu. Rev. Astron. Astrophys. **50**, p305 (2012).
19. P.-Y. Madec, "Overview of deformable mirror technologies for adaptive optics and astronomy," in *Int. Society for Optics and Photonics, Adaptive Optics Systems III,* , vol. 8447 (2012).
20. J.-F. Layerle, X. Savatier, E. Mouaddib, and J.-Y. Ertaud, "Catadioptric sensor for a simultaneous tracking of the driver's face and the road scene," in *8th Workshop on Omnidirectional Vision, Camera Networks and Non-classical Cameras,* (2008).
21. A. Ghorayeb, A. Potelle, L. Devendeville, and E. M. Mouaddib, "Optimal omnidirectional sensor for urban traffic diagnosis in crossroads," in *IEEE Intelligent Vehicles Symposium,* (2010), pp. 597–602.
22. R. Swaminathan, S. Nayar, and M. Grossberg, "Designing mirrors for catadioptric systems that minimize image errors," in *5th Workshop on Omnidirectional Vision,* (2004).
23. J. S. Gill, M. Moosajee, and A. M. Dubis, Nat. Publ. Group, Eye **33**, pp. 1683 (2019).
24. ISO®, "ISO 9039:2008 Optics and photonics – Quality evaluation of optical systems – Determination of distortion," (2008).
25. F. Faure, C. Duriez, H. Delingette, *et al.*, Soft tissue biomechanical modeling for computer assisted surgery, pp. 283–321 (2012).
26. B. Biswas, S. Chatterjee, S. Mukherjee, and S. Pal, Electron. J. Math. Anal. Appl. **1**, pp. 2090 (2013).
27. J. Allard, S. Cotin, F. Faure, *et al.*, "Sofa-an open source framework for medical simulation," in *IOP Press, Medicine Meets Virtual Reality,* , vol. 125 (2007), pp. 13–18.